POLITECNICO DI TORINO
Repository ISTITUZIONALE

Measuring and predicting pore size distribution of freeze-dried solutions

Original
Measuring and predicting pore size distribution of freeze-dried solutions / Arsiccio, A., Sparavigna, A.C., Pisano, R., Barresi, A.A.. - In: DRYING TECHNOLOGY. - ISSN 0737-3937. - STAMPA. - 37:4(2019), pp. 435-447. [10.1080/07373937.2018.1430042]

Availability:
This version is available at: 11583/2705512 since: 2020-01-23T22:23:11Z

Publisher:
Taylor and Francis Inc.

Published
DOI:10.1080/07373937.2018.1430042

Terms of use:

This article is made available under terms and conditions as specified in the corresponding bibliographic description in the repository

Publisher copyright
Taylor and Francis postprint/Author's Accepted Manuscript

This is an Accepted Manuscript of an article published by Taylor & Francis in DRYING TECHNOLOGY on 2019, available at http://wwww.tandfonline.com/10.1080/07373937.2018.1430042

(Article begins on next page)

13 September 2026

To cite this article:

A. Arsiccio, A. C. Sparavigna, R. Pisano & A. A. Barresi (2019) Measuring and predicting pore size distribution of freeze-dried solutions, *Drying Technology,* **37**(4), *435-447, DOI: 10.1080/07373937.2018.1430042*

To link to this article: https://doi.org/10.1080/07373937.2018.1430042

MEASURING AND PREDICTING PORE SIZE DISTRIBUTION OF FREEZE-DRIED SOLUTIONS*

A. Arsiccio, A.C. Sparavigna, R. Pisano, A.A. Barresi

Department of Applied Science and Technology, Politecnico di Torino

24 corso Duca degli Abruzzi, Torino, 10129 Italy

[*]*E-mail of the corresponding author:* antonello.barresi@polito.it

short title: MEASURING AND PREDICTING PORE SIZE DISTRIBUTION

Keywords: freeze drying, image analysis, mathematical modeling, pore structure

*This work summarizes and extends the two papers presented in the *Proceedings of 6th European Drying Conference - EuroDrying'2017,* Liège, Belgium, 19-21 June 2017: Arsiccio et al., Prediction of ice crystal size distribution during freezing of a pharmaceutical solution; Sparavigna et al., Measuring the size of pores by the segmentation of images from scanning electron microscopy.

Abstract: In this work, a novel procedure is presented for the measurement and prediction of pore size distribution of freeze-dried solutions in vials. A method based on segmentation is proposed for determining the size of the pores left by ice crystals, using images obtained by Scanning Electron Microscopy. The original ice crystal size distribution is also predicted using a mathematical model based on balance equations. The model predictions and the results of the segmentation technique show a fairly good agreement. The proposed procedure could be used to efficiently estimate the resistance to mass transfer during drying and hence optimize the freeze-drying process.

Introduction

The freeze-drying process is currently used as a common industrial processing and preservation technique, applied to a wide variety of products, the large part of them being foodstuffs, bio-products and pharmaceuticals. Consequently, the freeze-drying process has a high impact on industry and society.

Because of this fundamental role, research on freeze-drying is attracting the efforts of several scientific disciplines, rendering it the subject of a highly interdisciplinary area of studies.

The freezing step is actually the less investigated and understood, even though it strongly affects the following drying steps and the final quality of the product. In fact, the dimension of the ice crystals (or more generally of the solvent crystals) formed at this stage in the product to be freeze-dried is a critical aspect [1, 2, 3, 4], as it is linked to thermal stresses for the product, processing time [5, 6], product quality attributes, and inter- and intra-vial heterogeneity [6, 7].

In case of freeze-drying of solutions, in particular, the final pore structure of the matrix is mainly responsible for the resistance to vapor flow during primary drying, and for the desorption rate during secondary drying. Larger crystals, in fact, will result in larger pores and, thus, in a shorter primary drying, while secondary drying will be longer. This has been proven experimentally, evidencing also that obtaining larger pores by controlled nucleation may be beneficial, as it may finally lead to a reduced total processing time [8].

This explains recent interest for controlled ice nucleation in freeze-drying research, which has been proven to improve batch uniformity and may allow process optimization and process intensification [9]. The most interesting techniques, suitable for or already tested in industrial applications are the ice-fog [10, 11], the depressurization [12, 13, 14] and the vacuum induced nucleation [15, 16, 17].

The knowledge and control of the pore structure (pore shape, pore size distribution, and its variation within the product volume) or at least of the average pore size, may be very useful not only for allowing process optimization, but also for safe process transfer and scale up. In fact, all the model-based methods to predict the design space for primary drying [18, 19] and for both in-line and off-line process optimization [20, 21, 22], require knowledge (or in-line estimation) of the cake resistance to vapor flow.

This modeling approach is particularly complex in case of scale up and process transfer. In fact, in different pieces of apparatus or when different conditions are used (in particular GMP or not-GMP conditions), ice nucleation can occur differently, leading to different cake resistances and, thus, to different product temperatures during drying, or different drying duration. The use of models would allow optimization of the cycle, if the cake resistance obtained in the different conditions is known [23, 24]. The use of a lyobalance [20, 25], of thermocouples inserted into the product [26, 27, 28, 29], the direct measurement of the sublimation flux (coupled with knowledge of the heat transfer coefficient) [30] or the Pressure Rise Test, coupled with a suitable model [31, 32], are the methods usually employed for estimating the cake resistance during a freeze-drying cycle. However, these approaches are not generally available in industrial apparatus or compatible with GMP requirements.

An interesting alternative is the analysis of freeze-dried samples using micro-computed X-ray tomography (micro-CT) [33] or scanning electron microscopy (SEM) [34]. These techniques allow recovery of the required information without the necessity of expensive and time-consuming experiments, and the risk of altering the real processing conditions. To this scope it is also necessary to improve model prediction for cake resistance based on pore size information. In this regard, current approaches have shown promising results [34, 35 and 36], but they all still strongly rely on fitting parameters.

In perspective, the final goal of the current research is both the prediction of the final pore structure of the product as a function of the freezing operating conditions, and the evaluation of the mass transfer resistance from pore size information. To reach this goal, it is also necessary to develop an efficient way to recover the required information on pore structure form micro-CT or SEM analysis. All the model based approaches can thus receive a large benefit from improved techniques of image processing.

Several methods can be proposed for image analysis; in particular, the classical bi-dimensional Fourier Transform (2D-FFT) has been selected for this particular application in a previous work due to its easiness and to the possibility of directly relating the results to the spatial characteristics of the cake surface [37]. The approach based on the image wavelet decomposition followed by a non-linear processing based on an artificial neural network resulted to be a faster and more accurate solution, and in addition it did not require a model to link the cake surface porosity with the mass transfer coefficient [34, 38].

Here, we are proposing a method based on segmentation [39] for analyzing SEM images of dried products; it is often used in many applications of image processing, in particular in the medical image processing, where the aim is that of determining the presence of pathologies, and for the stacking of the maps coming from tomography to obtain 3D reconstructions [40, 41].

Segmentation is an image processing method used for partitioning an image into multiple sets of pixels, which are defined as its “super-pixels”. The dimension of pores, which corresponds to the size of ice crystals, is estimated through the areas of the super-pixels of the segmented image.

Results obtained from image processing are compared with predictions of a mathematical model, which substantially differs from previous approaches. In fact, equations proposed so far to correlate the crystal size with the product thermal history during freezing are based on empirical formulas and lack of physical explanation. Many of such works relate the crystal dimension, D_p, with the temperature gradients within the frozen zone θ and the freezing front velocity v:

$$D_p = \alpha\, \theta^{-\lambda_1}\, v^{-\lambda_2} \tag{1}$$

where α, λ_1 and λ_2 are adjustable coefficients that vary according to the type of product and process, and that sometimes change even within the same application. In literature, the values -0.5 or -1 have been proposed for λ_1 (but the dependence on θ has also sometimes been neglected), while λ_2 ranges from -0.25 to -1 [42, 43, 44]. For pharmaceutical solutions, the value -0.5 for both exponents, as originally proposed by Bomben and King for freezing of apples [42], has been employed in previous modeling works [36, 45].

On the contrary, in this work we employ a mechanistic model capable of providing physical insight into the process and of predicting the ice crystal size distribution in wide ranges of conditions. The model has been developed in both a detailed and a simplified version [46], but we will focus here on the simplified one. The simplified model is easier to be implemented, but it is valid for dilute solutions only. In spite of this limitation, it was able to predict with good accuracy the ice crystals dimension of typical pharmaceutical formulations.

Combination of the image processing technique and of the mathematical model proposed could be extremely beneficial for the modeling and optimization of the freeze-drying process.

Image segmentation

As previously stated, in image processing, segmentation is the process of partitioning an image into multiple sets of pixels, defined as super-pixels, in order to have a representation which is simpler than the original one and more useful for the following desired analyses.

The typical use of image segmentation is that of locating objects, or domains, and boundaries among them. More specifically, segmentation is the process of assigning a label to every pixel in an image, such that pixels having the same label share certain characteristics. As a consequence, the result of segmentation is a set of "segments", or “super-pixels”, that are covering the whole image. Several methods exist for segmentation, mainly based on the use of binary (black and white) images (see, for instance, [47]).

In general, we have a color RGB source image of $N_x \times N_y$ pixels, represented by the three-channel brightness function $b_c : I \to B$, where $I = [1, N_x] \times [1, N_y] \subset \mathbb{N}^2$ and $B = [0,255]^3 \subset \mathbb{N}^3$. From this function, a grey-tone map can be obtained as follows,

$$\tilde{\beta}(i, j) = \frac{1}{3} \sum_{c=1}^{3} b_c(i, j) \tag{2}$$

The index *c* corresponds to the three RGB channels. The integer indices *i* and *j* are ranging in the *x* and *y* directions of the Cartesian frame corresponding to the image frame. In this way, a brightness map of grey-tone pixels can be obtained.

The images that we are here considering are coming from a SEM instrument and therefore have already grey-tone pixels. Our aim is that of measuring the size of the pores, which are, in the SEM images, represented by dark or black pixels. Thus, in the segmentation of the image, a method for the thresholding of the brightness map must be defined. The thresholding is carried out using a clip-level (the threshold value τ), according to which a grey-scale image is turned into a binary image *T(i,j)*.

$$\begin{aligned} &\tilde{\beta}(i, j) \le \tau \to T(i, j) = 0 \quad black \\ &\tilde{\beta}(i, j) > \tau \to T(i, j) = 255 \; white \end{aligned} \tag{3}$$

The clip-level has a crucial role in the rendering of the binary image; often it is determined by means of the entropy, evaluated on the histogram of grey-tones of the pixels [48, 49, 50].

In the case of SEM images, we preferred using a software such as GIMP (GNU Image Manipulation Program, for X Windows systems) and making a visual choice of thresholding. Usually, it is necessary to equalize the histogram of the grey-tones of the SEM image, before converting the image into a binary one. Sometimes, other tools of GIMP are necessary to have a further adjustment of the binary image, as we will discuss in the following given examples. Once we have obtained the binary image, we have at our disposal a matrix of pixels containing black and white domains. Starting from the left/upper corner of this matrix, we can thus move following rows and columns of the matrix. We focus on black pixels and characterize each of them by a sequential integer number *k*, which is acting as a label of the single pixel. Some of these labels will be the labels identifying the domains, or super-pixels, to which the pixels belong (see Figure 1).

The label of a black pixel is determined according to the labels *k* of the nearest black pixels above (A) and on the left (L) of the considered pixel. If the labels k_A and k_L are the same, their value is the label of the pixel under examination. If these labels are different, the pixel assumes as its label the lower value among them. Then, all the pixels having the label with the larger value change their labels into the value of the smaller one (see Figure 1). This approach can be easily obtained by logic instructions in any programming language (here we used Fortran 77).

First, the binary image is converted into .ppm ascii file. This file is easily read by Fortran and the image is converted into a 2x2 matrix. Once this matrix has been obtained, the following algorithm is applied. The algorithm gives to each of the super-pixel a different label, generating a matrix of labels:

$$\begin{aligned} &T(i, j) = 255 \to K(i, j) = 0 \\ &T(i, j) = 0 \quad \to \quad K(i, j) = k, \; k \ne 0, k \subset \mathbb{N} \end{aligned} \tag{4}$$

Then, a new map can be proposed, where a color tone is associated to such labels and, therefore, to each super-pixel, such as in the example given in Figure 2. Since each black pixel of the original grey-tone image has the label of the super-pixel to which it belongs, we can easily do some calculations. First of all, we have the number of the super-pixels. Then, for each of them, we can give the number of pixels, that is, the area (in pixels) the super-pixel is covering, as shown in Figure 2.

The world of image segmentation is very wide, but, to the best of our knowledge, our approach is substantially different from previous ones. For example, the proposed algorithm is inspired, as Figure 1

shows, by crossword puzzles. In our case, the words are the black domains characterized by a single label. Solving the puzzle means determining the label of each domain. A recently proposed crossword algorithm, based on an iterative k-means clustering [51], is however considerably different from the approach given here. Actually, our algorithm is closer to those concerning the solution of QR codes [52], but the differences between these codes and the one proposed in the present paper remain in any case remarkable.

Mathematical model

The domain under investigation is the cylinder of product, having height Δz and diameter D, where crystal growth is occurring. A picture of the domain under investigation, which corresponds to a slice of the product in the vial, is shown in Figure 3.

In order to determine ice crystals size, an energy balance is written that describes the crystal growth process, once nucleation occurred. The domain considered changes its position during the process, as it follows the freezing front. Thus, the product height needs to be discretized into a finite number n of intervals, which will be denoted by subscript i.

During the process, the temperature of the freezing front and of the zone where freezing has not yet completed is almost constant and equal to the equilibrium value. So, it is reasonable to model our domain considering steady state conditions, as well as absence of energy exchange with the unfrozen zone. Thus, the following energy balance, which applies to the crystal growth phase, can be written:

$$\begin{pmatrix} heat\ removed \\ by\ the \\ frozen\ product \end{pmatrix} + \begin{pmatrix} heat\ transferred \\ from\ the \\ lateral\ surface \end{pmatrix} + \begin{pmatrix} heat\ released \\ by \\ ice\ crystallization \end{pmatrix} + \begin{pmatrix} enthalpy\ change \\ due\ to\ new \\ interface\ generation \end{pmatrix} = 0$$

$$-k_s\theta_i\pi\frac{D^2}{4} - \pi D\Delta z h\Delta T + \frac{dV_{ice,i}}{dt}\rho_{ice}\Delta H_f - \frac{dS_{ice,i}}{dt}\gamma = 0 \tag{5}$$

The last term of Equation 5, related to generation of new solid-solid surfaces, is significant and cannot be neglected. In fact, simulations have proven that it can contribute up to 50% to removal of heat released by ice crystallization.

The derivatives in Equation 5 can be approximated by the corresponding finite increments,

$$\frac{dV_{ice,i}}{dt} = \frac{\Delta V_{ice,i}}{\Delta t_i} = \frac{N_i\pi D_{p,i}^2\tilde{\tau}\Delta z}{4\Delta t_i} = \frac{N_i\pi D_{p,i}^2\tilde{\tau}v_i}{4} \tag{6}$$

$$\frac{dS_{ice,i}}{dt} = \frac{\Delta S_{ice,i}}{\Delta t_i} = \frac{N_i\pi D_{p,i}\tilde{\tau}\Delta z a_{S,i}}{\Delta t_i} = N_i\pi D_{p,i}\tilde{\tau}a_{S,i}v_i \tag{7}$$

In Equations 6 and 7, we assumed the pores to be cylinders with constant diameter $D_{p,i}$ in Δz, and neglected the initial volume and surface of crystal nuclei. The tortuosity value $\tilde{\tau}$ must be introduced to take into account that pores are inclined from the vertical axis, and the inclination angle δ is linked to the tortuosity by the relation $\tilde{\tau} = \cos\delta^{-1}$. The freezing front velocity, v_i, is defined as $v_i = \Delta z/\Delta t_i$, while $a_{S,i}$ is the ratio between the real ice surface area and the fictitious one calculated considering the ice crystals as perfect and smooth cylinders,

$$a_{S,i} = \frac{real\ surface\ area}{N_i\pi D_{p,i}\tilde{\tau}\Delta z} \tag{8}$$

By substitution of Equations 6 and 7 into Equation 5, we obtain

$$-k_s\theta_i\pi\frac{D^2}{4} - \pi D\Delta z h\Delta T + N_{p,i}\pi\frac{D_{p,i}^2}{4}\rho_{ice}\tilde{\tau}v_i\Delta H_f - N_{p,i}\pi D_{p,i}\tilde{\tau}v_i\gamma a_{S,i} = 0 \tag{9}$$

We can then combine the energy balance with the following mass balance,

$$\sum_{i=1}^{n} N_{p,i}\pi\frac{D_{p,i}^2}{4}\rho_{ice}\tilde{\tau}\Delta z = m \tag{10}$$

where m is the mass of water which crystallizes.

If we then assume that the mass of ice which crystallizes is proportional to the heat removed, we obtain the following equation,

$$D_{p,i} = \frac{16m\theta_i\gamma b\nu_i}{\rho_{ice}\theta_i^{2/3}(4m\theta_i\nu_i\Delta H_f - k_s\theta_i D^2\pi\Delta z\sum_{i=1}^{n}\theta_i - 4\pi\Delta^2 z\sum_{i=1}^{n}\theta_i Dh\Delta T)} \tag{11}$$

where the term b accounts for surface irregularities and the real ice crystal habit. This is the general result of the model.

However, if we assume that the solution is dilute, the model can be further simplified. More specifically, if the water content is very high, we can assume that the term ND_p is large and, hence, the second term in Equation 5, i.e., heat transferred from the lateral surface, is negligible with respect to the others.

Moreover, we could write the following approximated mass balance:

$$\varepsilon\pi\frac{D^2}{4} \approx N_{p,i}\pi\frac{D_{p,i}^2}{4}\tilde{\tau} \tag{12}$$

where ε is the ratio between the volume of ice and the total volume of the system.

If we make these two approximations, we obtain a simpler equation:

$$D_{p,i} = \frac{4\varepsilon\gamma b\nu_i}{(\varepsilon\rho_{ice}\nu_i\Delta H_f - k_s\theta_i)\theta_i^{2/3}} \tag{13}$$

Equation 13 is valid for dilute solutions only, but we previously showed [46] that it can be effectively applied to the freeze-drying of all typical pharmaceutical formulations, whose solid content is generally lower than 10%. Moreover, if the solution is not sufficiently dilute, Equation 11, in which no simplifications were introduced, could be used.

The product γb cannot be calculated theoretically and has therefore to be estimated by fitting of experimental data for crystal size vs. product thickness. However, it has a physical meaning and was found to be independent of operating conditions, such as cooling rate and nucleation temperature. This means that a single experiment needs to be carried out for each formulation, at any desired operating conditions. Then, the model allows evaluation of the pore size distribution resulting from any other possible choice of freezing conditions and/or freezing protocol. Moreover, the empirical laws previously proposed for prediction of pore size distribution [42-45], despite using from 2 to 3 fitting parameters, allowed prediction in a limited range of operating conditions, without providing any insight into process behavior. Thus, the increased range of validity and the clear meaning of all terms involved are other strengths of the mechanistic model.

We will focus here on the simplified model, Equation 13, which is easier to implement. Details on validation of the complete model for conventional and controlled nucleation can be found elsewhere [46].

Materials and Methods

The image segmentation technique and the mathematical model were validated using two different solutes, mannitol and sucrose, which represent an amorphous and a crystalline system respectively. Mannitol and sucrose were purchased from Sigma Aldrich and used as supplied. The vials employed (type 1, 10R, 45x24 mm, Schott AG, Germany) were accurately filled with 3 ml of sample solution. A freeze-dryer LyoBeta 25 (Telstar, Terrassa, Spain) was used for the freeze-drying cycles. In order to monitor the temperature of the shelves and of the product a system of T-type copper/constantan miniature thermocouples was used.

The experiments were performed using the traditional shelf-ramped freezing technique. The vials were loaded onto the freeze-dryer shelves and then the refrigerating fluid temperature was decreased with a precise cooling rate until a value of -45°C was reached. Table 1 lists the details of formulations and operating conditions investigated.

After freeze-drying, the pore dimension of the product obtained, which corresponds to the ice crystal size formed after freezing, was evaluated using SEM analysis (SEM, FEI type, Quanta Inspect 200, Eindhoven, the Netherlands). The specimens were metalized and for each sample, three images were taken at the top, center, and bottom of the product; the problems connected with the image acquisitions have been already discussed in detail [34].

Images obtained by Scanning Electron Microscopy were processed using the image segmentation technique previously described. Moreover, in order to have a reference value, SEM images were analyzed using the traditional technique adopted in a previous work [46]; that is, a large number (approximately 100) of pores per image was selected and each pore was approximated to an ellipse. The dimension, D_p, we attributed to the pore, was the diameter of the circle having the same area to perimeter ratio of the approximating ellipse.

The product temperature profiles during freezing were obtained using the model developed by Nakagawa et al. and Pisano and Capozzi [36, 45] and compared with the experimental value. The 2D axisymmetric model for temperature prediction was solved using the commercial software COMSOL Multiphysics. While the experimental measure provided the temperature value at a single point of the sample, Nakagawa's model allowed the estimation of temperature within the whole product, providing the information required for the evaluation of v and θ. In fact, at the freezing front the temperature is equal to the equilibrium value and thus its position can be easily known; thus, v can be evaluated as the ratio between the variation of the freezing front position Δz_f and the time interval Δt

$$v = \frac{\Delta z_f}{\Delta t} \tag{14}$$

The temperature gradient θ is equal to the slope of the curve, at a given time, below the equilibrium freezing temperature.

Results and discussion

To estimate the size of the pores, we processed the SEM images using the segmentation approach outlined in the previous section.

Let us consider mannitol 5% w/w, test A in Table 1. Using SEM, three images of the dried cake were taken at top, center and bottom, see Figure 4a. We determined the thresholding using GIMP and visual inspection of the SEM images, to obtain the binary images from the grey-tone original ones, Figure 4b. A smoothing was required, to avoid the presence of a multitude of domains containing few black pixels. The smoothing was obtained applying the GIMP filter, which simulates the brushstrokes of oil painting. Since the filter applied to remove the small domains also removes the thin walls between pores, to restore them we used the binary watershed tool of ImageJ, a public domain Java-based image program.

Once the image is segmented, Figure 4c, it is possible to deduce the area of each pore from the area of the corresponding super-pixel. Then, we can plot the distribution of the super-pixels, and consequently the occurrences N of them, for given areas of the pores within intervals spaced of 100 pixels (Figure 4d). As it is possible to notice, the presence of large pores is sensibly reduced in the bottom of the cake.

For what concerns the real size of the pores, that is, in microns and not in pixels, we can use the scale given by the SEM images. Assuming roughly a circular section of the pores, we can calculate an effective radius of the pore. Let us consider the peaks in Figure 4d, as indicated by white arrows. These peaks correspond to the mode of the pore distribution, as measured by the image segmentation approach. For the top of the cake, the peak corresponded to an area of 1150 pixels, giving a radius of about 25 microns. In the center, two peaks can be observed in Figure 4d. One corresponded to an area of 1350 pixels, and then to a radius of 27 microns. The other peak corresponded to an area of 1600 pixels and then to a radius of about 30 microns. In the bottom of the cake, the peak corresponded to an area of 900 pixels, and then of a radius of about 23 microns.

As we did for mannitol, we repeated the segmentation for three SEM images of a cake of sucrose 5% w/w (test B in Table 1). In Figures 5a-b, the original SEM images and the binary images are shown. The plots in Figure 5c give the distribution of the super-pixels, and consequently the occurrences N of them, for given areas of the pores within intervals spaced of 100 pixels. In this case, the presence of large pores seems to be sensibly reduced in the top of the cake.

Again, for what concerns the real size of the pores, we can use the scale given by the SEM images. Assuming roughly a circular section of the pores, we can give an effective radius of the pore. In Figure 5c, the peaks corresponding to the mode of the distribution are again indicated by white arrows. For the top of the cake, the peak corresponded to an area of 1200 pixel, giving a radius of about 35 microns. In the center, the peak corresponded to an area of 3300 pixels, and then to a radius of 55 microns. In the bottom of the cake, the peak corresponded to an area of 2700 pixels, and then to a radius of about 50 microns.

In Table 2, results obtained by image segmentation are compared with those obtained by the traditional image analysis technique. As it is possible to notice, the accordance is very good for the formulation containing mannitol, while for the sucrose-based one the image segmentation technique predicted pore dimensions which were in any case smaller than those measured by the traditional technique. This could be explained considering that the traditional method gives as output the numerical average of the distribution, while the image segmentation technique produces the mode of the same distribution. However, while the numerical value of the mode is the same as that of the mean in a normal distribution, it may be very different, and generally flattened on lower values, in highly skewed distributions. This could explain the difference between the two techniques in the case of the sucrose formulation. Nevertheless, the image segmentation approach could reproduce the trend evidenced by the traditional method, with the sucrose formulation having bigger pores than the mannitol one and with the center of the cake having bigger pores than the top and the bottom.

As regards the mathematical model for prediction of ice crystal size, in this work we focused on the simplified approach, Equation 13. The aim is to demonstrate its validity for formulations and operating conditions which are usually employed for pharmaceuticals.

The values of the parameters used in the model are listed in Table 3.

As can be seen from the Table, the numerical value of parameter γb is much higher for sucrose than for mannitol. Another amorphous solute, dextran, has been found to have the same γb coefficient as sucrose [46].

Figure 6 shows that for both solutes, tests A and B, the model predicted fairly well the crystal size distribution as measured experimentally by SEM analysis.

The model was then tested for different operating conditions and concentration, but using mannitol as model solute. More specifically, nucleation temperature, cooling rate and concentration were changed. The product morphology, as measured using the traditional SEM analysis approach and as predicted by the model, was characterized using the crystal diameter averaged over the vertical direction. As can be seen in Table 4, the simplified model could predict with good accuracy the product morphology.

Tests A and C were performed using the same cooling rate, but the two samples had different nucleation temperatures. On the contrary, tests A and D had similar nucleation temperatures but were conducted using very different cooling rates. As can be seen from the Table, the model could effectively predict the crystal size increase with increasing nucleation temperature (tests A and C), and with decreasing cooling rate (tests A and D). In fact, nucleation temperature and cooling rate are taken into account by the model in the v and θ terms.

Moreover, it is remarkable that the model worked fairly well even at the higher concentration of 10% w/w employed for test E. This means that the simplified model can be effectively applied to typical pharmaceutical formulations, whose concentration is generally smaller than 10% w/w.

The image segmentation approach and the mechanistic model here presented, make it possible to know the whole pore size distribution within the product thickness. This is important for determination of a suitable mass transfer resistance to vapor flux, to be used in models of primary drying [53, 54]. For example, the sample could be divided into vertical sections, and a mean value of D_p could be attributed to each section. Using this value of D_p, a mass transfer resistance could be calculated for each of the selected sections. Subsequently, the values of mass transfer resistance calculated for

different sections could be considered as elements of a connection in series and summed up to give the resistance of the whole sample. This procedure could improve determination of a reasonable value for mass transfer resistance, especially for those formulations and operating conditions which tend to form very inhomogeneous cakes. By contrast, radial inhomogeneity in pore distribution is much more difficult to take into account. Thus, at present, it is not easy to translate this complexity into a compact analytical expression for the mass transfer resistance, suitable for conventional models of primary drying.

Let us conclude mentioning the advantages of the image segmentation approach here proposed. In the case of the traditional approach, the time required for analysis of each image is ranging from 30 min to 1 h, depending on the number of pores which have to be analyzed. Moreover, this approach provides results which depend on the sensibility of the person who is performing the analysis. This means that reliability of data obtained cannot be always guaranteed. By contrast, in the case of an automatized approach, time is considerably reduced, and reliability of the results obtained is improved. The only drawback is the proper choice of the thresholding value. Here, visual inspection was used to obtain reliable results, even if a choice based on maximum image entropy is under consideration for a fully automatized method [48-50]. However, we found that results of our algorithm were remarkably stable and were thus not dramatically influenced by choice of the threshold. For example, ImageJ was found to be more sensitive to changes in the thresholding value. Future work will quantitatively compare the role of the threshold in both approaches. Moreover, comparison with the results obtained by means of an algorithm based on wavelets is also under development [38].

According to the results obtained, the segmentation algorithm proposed in this paper could be really beneficial, and allow a more reliable analysis of images in a wide variety of fields. In fact, even if it was developed and validated for freeze-dried products, the proposed approach could also be effectively used for analysis of porous media in general, or whenever difficulties in detection of clear edges impede use of other techniques.

Conclusions

As we have illustrated, the study of the pores of lyophilized samples can be remarkably improved by image processing. Here, for instance, we have determined the segmentation of the super-pixels which are containing the pores, in order to estimate their size. Let us add that the approach we have used, namely, segmentation, is the first step for any further 3D reconstruction of the sample from images given by tomography.

Moreover, a simplified model for the prediction of ice crystal size distribution in frozen products has been discussed. Unlike previous approaches, which were completely empirical, the model here presented provides physical insight into process phenomena.

The model predictions have been validated upon experimental observations collected by analysis of SEM images. The validation has been performed for different operating conditions and concentrations, showing that the simplified model developed can be efficiently applied to typical pharmaceutical solutions.

Knowledge of the average pore size and its distribution is essential for the determination of the resistance to mass transfer and hence for the use of the most recent model-based tools for the development and scale-up of freeze-drying cycles. The approach here developed is therefore a solid starting point for a more efficient design of the freeze-drying process.

However, not all the problems have been solved. In the model developed there still is a term that must be evaluated from experimental data. Thus, further work is needed to make crystal size completely predictable from theoretical considerations, without need of experiments.

List of Symbols

a_S	empirical coefficient that accounts for the real ice crystals surface, -
b	coefficient that accounts for surface irregularities and crystal habit, $K^{2/3}\ m^{-2/3}$
b_c	three-channel brightness function, -
B	image of the three-channel brightness function, -
c	index corresponding to the three RGB channels, -

D	vial base diameter, m
D_p	crystals diameter, m
h	heat transfer coefficient, W m^{-2} K^{-1}
I	domain of the three-channel brightness function, -
ΔH_f	latent heat of crystallization, J kg^{-1}
k	pixel label, -
k_s	thermal conductivity of the solid, W m^{-1} K^{-1}
$K(i,j)$	matrix of labels, -
m	mass of crystallized water, kg
n	number of discretization intervals, -
N	number of occurrences of super-pixels with a given area, -
N_p	number of crystals, -
N_x	number of pixels in the x direction, -
N_y	Number of pixels in the y direction,-
S_{ice}	surface of ice crystals, m^2
T	temperature, K
$T(i,j)$	binary image map, -
ΔT	temperature difference between air and product, K
t	time, s
Δt	time interval, s
V_{ice}	volume of ice crystals, m^3
z	axial coordinate, m
z_f	axial coordinate of the freezing front, m
Δz	axial interval, m
Δz_f	variation of the freezing front position, m

Greek letters

α	empirical coefficient of Equation 1, -
$\tilde{\beta}(i,j)$	grey-tone map, -
γ	solid-solid interfacial tension, J m^{-2}
ε	ratio between the volume of ice and the total volume of the system, -
θ	temperature gradient within the frozen zone, K m^{-1}
λ_1	exponent of Equation 1, -
λ_2	exponent of Equation 1, -
v	freezing front velocity, m s^{-1}
ρ_{ice}	density of ice, kg m^{-3}
τ	threshold value for binary image construction, -
$\tilde{\tau}$	tortuosity value, -

Abbreviations

GIMP	GNU Image Manipulation Program, -

References

[1] Franks, F.; Auffret, T. Freeze-Drying of Pharmaceuticals and Biopharmaceuticals; RCS Publishing: Cambridge, UK, 2007.

[2] Rey, L.; May, J. Freeze-Drying/Lyophilization of Pharmaceuticals and Biological Products; Marcel Dekker, Inc: New York, USA, 2004.

[3] Hottot, A.; Vessot, S.; Andrieu, J. Freeze-drying of pharmaceuticals in vials: influence of freezing protocol and sample configuration on ice morphology and freeze-dried cake texture. Chemical Engineering and Processing: Process Intensification 2007, 46 (7), 666-674.

[4] Oddone, I.; Fulginiti; D., Barresi; A.A., Pisano; R., Grassini, S. Non-invasive temperature monitoring in freeze drying: control of freezing as a case study. Drying Technology 2015, 33 (13), 1621-1630.

[5] Searles, J.; Carpenter, J.; Randolph, T. The ice nucleation temperature determines the primary drying rate of lyophilization for samples frozen on a temperature-controlled shelf. Journal of Pharmaceutical Sciences 2001, 90 (7), 860-871.
[6] Kasper, J.C.; Friess, W.F. The freezing step in lyophilization: Physico-chemical fundamentals, freezing methods and consequences on process performance and quality attributes of biopharmaceuticals. European Journal of Pharmaceutics and Biopharmaceutics 2011, 78 2): 248–63.
[7] Oddone, I.; Van Bockstal, P.-J.; De Beer, T.; Pisano, R. Impact of vacuum-induced surface freezing on inter- and intra-vial heterogeneity. European Journal of Pharmaceutics and Biopharmaceutics 2016, 103 (1), 167-178.
[8] Oddone, I.; Barresi, A.A.; Pisano, R. Influence of controlled ice nucleation on the freeze-drying of pharmaceutical products: the secondary drying step. International Journal of Pharmaceutics 2017, 524 (1-2), 134-140.
[9] Pisano, R.; Fissore, D.; Barresi, A.A.; Intensification of freeze-drying for the pharmaceutical and food industry. In: Modern Drying Technology Vol. 5: Process Intensification; Tsotsas, E., Mujumdar, A.S., Eds.; Wiley-VCH Verlag GmbH & Co. KGaA: Weinhein, 2014; Chap. 5, pp. 131-161.
[10] Patel, S.; Bhugra, C.; Pikal, M. Reduced pressure ice fog technique for controlled ice nucleation during freeze-drying. AAPS PharmSciTech 2009, 10, 1406−1411.
[11] Rambhatla, S.; Ramot, R.; Bhugra, C.; Pikal, M.J. Heat and mass transfer scale-up issues during freeze drying, Part 2: Control and characterization of the degree of supercooling. AAPS PharmSciTech 2004, 5 (4), No. 58.
[12] Rampersad, B.M.; Sever, R.R.; Hunek, B.; Gasteyer, T.H. Freeze-dryer and method of controlling the same. U.S. Patent Application Publication US 824065 B2, 2012.
[13] Bursac, R.; Sever, R.; Hunek, B. A practical method for resolving the nucleation problem in lyophilization. Bioprocess International 2009, 7 (9), 66–72.
[14] Konstantinidis, A.K.; Kuu, W.; Otten, L.; Nail, S.L.; Sever, R.R.,. Controlled nucleation in freeze-drying: Effects on pore size in the dried product layer, mass transfer resistance, and primary drying rate. Journal of Pharmaceutical Science 2011, 100 (8), 3453–3470.
[15] Kramer, M.; Sennhenn, B.; Lee, G. Freeze-drying using vacuum-induced surface freezing. Journal of Pharmaceutical Science 2002, 91, 433−443.
[16] Liu, J.; Viverette, T.; Virgin, M.; Anderson, M.; Dalal, P.A study of the impact of freezing on the lyophilization of a concentrated formulation with a high fill depth. Pharmaceutical Development and Technology 2005, 10, 261−272.
[17] Oddone, I.; Pisano, R.; Bullich, R.; Stewart, P. Vacuum-induced nucleation as a method for freeze-drying cycle optimization. Industrial & Engineering Chemistry Research 2014, 53 (47), 18236-18244.
[18] Giordano, A.; Barresi, A.A.; Fissore, D. On the use of mathematical models to build the design space for the primary drying phase of a pharmaceutical lyophilization process. Journal of Pharmaceutical Science 2011, 100 (1), 311-324.
[19] Fissore, D.; Pisano, R.; Barresi, A.A. Advanced approach to build the design space for the primary drying of a pharmaceutical freeze-drying process. Journal of Pharmaceutical Science 2011, 100 (11), 4922-4933.
[20] Fissore, D.; Pisano, R.; Barresi, A.A. A model based framework to optimize pharmaceuticals freeze-drying. Drying Technology 2012, 30, 946-958
[21] Pisano, R.; Fissore; D., Barresi, A.A. In-line and off-line optimization of freeze-drying cycles for pharmaceutical products. Drying Technology 2013, 31 (8), 905-919.
[22] Fissore, D.; Pisano, R. Computer-aided framework for the design of freeze-drying cycles: Optimization of the operating conditions of the primary drying stage. Processes 2015, 3 (4), 406-421.
[23] Pisano, R.; Fissore, D.; Barresi, A.A.; Rastelli, M. Quality by design: Scale-up of freeze-drying cycles in pharmaceutical industry. AAPS PharmSciTech 2013, 14 (3), 1137-1149.
[24] Fissore, D.; Barresi, A.A. Scale-up and process transfer of freeze-drying recipes. Drying Technology 2011, 29 (14), 1673-1684).

[25] Fissore, D.; Pisano, R.; Barresi, A.A. Model-based framework for the analysis of failure consequences in a freeze-drying process. Industrial & Engineering Chemistry Research 2012, 51 (38) 12386–12397.
[26] Kuu, W.-Y.; McShane, J.; Wong, J. Determination of mass transfer coefficients during freeze drying using modeling and parameter estimation techniques. International Journal of Pharmaceutics 1995, 124 (2-3), 241-252.
[27] Kuu, W.Y.; Hardwick, L.M.; Akers, M.J. Rapid determination of dry layer resistance to various pharmaceutical formulations during primary drying using product temperature profiles. International Journal of Pharmaceutics 2006, 313 (1), 99–113.
[28] Bosca, S.; Barresi, A.A.; Fissore, D. Use of a soft-sensor for the fast estimation of dried cake resistance during a freeze-drying cycle. International Journal of Pharmaceutics 2013, 451, 23-33.
[29] Bosca, S.; Barresi, A.; Fissore, D. Design of a robust soft-sensor to monitor in-line a freeze-drying process. Drying Technology 2015, 33 (9), 1039-1050.
[30] Kuu, W.Y.; Obryan, K.R.; Hardwick, L.M.; Paul, T.W. Product mass transfer resistance directly determined during freeze-drying cycle runs using tunable diode laser absorption spectroscopy (TDLAS) and pore diffusion model. Pharmaceutical Development and Technology 2011, 16 (4), 343–357.
[31] Hottot, A.; Vessot, S.; Andrieu, J. Determination of mass and heat transfer parameters during freeze-drying cycles of pharmaceutical products, PDA Journal of Pharmaceutical Science and Technology 2005, 59 (2), 138–153.
[32] Fissore, D.; Pisano, R.; Barresi, A.A. On the methods based on the Pressure Rise Test for monitoring a freeze-drying process. Drying Technology 2011, 29 (1), 73-90.
[33] Pisano, R.; Barresi, A.A.; Capozzi, L.C.; Novajra, G.; Oddone, I.; Vitale-Brovarone, C. Characterization of the mass transfer of lyophilized products based on X-ray micro-computed tomography images. Drying Technology 2017, 35(8), 933-938.
[34] Grassini, S.; Pisano, R.; Barresi, A.A.; Angelini, E.; Parvis, M. Frequency domain image analysis for the characterization of porous products. Measurement 2016, 94, 515-522.
[35] Kodama, T.; Sawada, H.; Hosomi, H.; Takeuchi, M.; Wakiyama, N.; Yonemochi, E.; Terada, K. Determination for dry layer resistance of sucrose under various primary drying conditions using a novel simulation program for designing pharmaceutical lyophilization cycle. International Journal of Pharmaceutics 2013, 452 (1–2), 180–187.
[36] Pisano, R.; Capozzi, L. Prediction of product morphology of lyophilized drugs in the case of Vacuum Induced Surface freezing. Chemical Engineering Research & Design 2017, 125, 119-129.
[37] Parvis, M.; Grassini, S.; Angelini, E.; Pisano, R.; Barresi, A.A. Characterization of freeze-dried pharmaceutical product structures by an FFT-imaging approach. In Proceedings of. IEEE International Symposium on Medical Measurements and Applications “MeMeA 2014”, Lisbon, Portugal, June 11-12, 2014; 302-307.
[38] Grassini, S.; Angelini, E.; Pisano, R.; Barresi, A.; Parvis M. Wavelet image decomposition for characterization of freeze-dried pharmaceutical product structures. In Proceedings of IEEE International Instrumentation and Measurements Technology Conference “I2MTC 2015”, Pisa, Italy, May 11-14, 2015; 2072-2077.
[39] Shapiro, L.G.; Stockman, G.C. Computer Vision; Prentice-Hall: New Jersey, 2001.
[40] Pham, D.L.; Xu, C.; Prince, J.L. Current methods in medical image segmentation. Annual Review of Biomedical Engineering 2000, 2 (2000), 315-337.
[41] Forghani, M.; Forouzanfar, M.; Teshnehlab, M. Parameter optimization of improved fuzzy c-means clustering algorithm for brain MR image segmentation. Engineering Applications of Artificial Intelligence 2010, 23 (2), 160-168.
[42] Bomben, J.L.; King, C.J. Heat and mass transport in the freezing of apple tissue. International Journal of Food Science & Technology 1982, 17 (5), 615-632.
[43] Kochs, M.; Korber, C.H.; Heschel, I.; Nunner, B. The influence of the freezing process on vapour transport during sublimation in vacuum freeze-drying. International Journal of Heat and Mass Transfer 1991, 34 (9), 2395-2408.
[44] Kurz, W.; Fisher, D.J. Fundamentals of Solidification; Trans Tech Publications: Switzerland,

1992.
[45] Nakagawa, K.; Hottot, A.; Vessot, S.; Andrieu, J. Modeling of freezing step during freeze-drying of drugs in vials. AIChE Journal 2007, 53 (5), 1362-1372.
[46] Arsiccio, A.; Barresi, A.A.; Pisano, R. Prediction of ice crystal size distribution after freezing of pharmaceutical solutions. Crystal Growth and Design 2017, 17 (9), 4573-4581.
[47] Schladitz, K. Quantitative micro-CT. Journal of Microscopy 2011, 243(2), 111-117.
[48] Gull, S.F.; Skilling, J. Maximum entropy method in image processing. IEE Proceedings F - Radar and Signal Processing 1984, 131(6), 646-659.
[49] Sahoo, P.K.; Arora, G. Image thresholding using two-dimensional Tsallis – Havrda – Charvát. Pattern Recognition Letters 2006, 27 (6), 520-528.
[50] Sparavigna, A.C. Tsallis entropy in bi-level and multi-level image thresholding. International Journal of Sciences 2015, 4(1), 40-49.
[51] Gierahn, T.M.; Loginov, D.; Love, J.C. Crossword: a fully automated algorithm for the segmentation and quality control of protein microarray images. Journal of Proteome Research 2014, 13(2), 362.
[52] Zigomitros, A.; Patsakis C; Cross format embedding of metadata in images using QR codes. In Intelligent Interactive Multimedia Systems and Services. Smart Innovation, Systems and Technologies; Tsihrintzis, G.A., Virvou, M., Jain, L.C., Howlett, R.J., Eds.; Springer: Berlin, 2011; 113-121.
[53] Bosca, S.; Barresi, A.A.; Fissore, D. Use of soft sensors to monitor a pharmaceuticals freeze-drying process in vials. Pharmaceutical Development and Technology 2014, 19(2), 148-159.
[54] Rambhatla, S.; Ramot, R.; Bhugra, C.; Pikal, M.J. Heat and mass transfer scale-up issues during freeze drying: II. Control and characterization of the degree of supercooling. AAPS PharmSciTech 2004, 5(4), 1-9.

Table 1. Details of experimental tests.

	Formulation	**Cooling rate, K min^{-1}**	**Nucleation temperature, K**
A	Mannitol 5% w/w	0.8	260.5
B	Sucrose 5% w/w	0.8	258.2
C	Mannitol 5% w/w	0.8	266.4
D	Mannitol 5% w/w	0.1	261.0
E	Mannitol 10% w/w	0.8	261.3

Table 2. Comparison between the traditional image analysis technique and the newly developed segmentation approach. Data given for segmentation are those corresponding to the arrows in the Figures 4 and 5.

		D_p, µm		
		Top	Centre	Bottom
Mannitol 5 % (Test A)	segmentation	25	27-30	23
	traditional	23	28	19
Sucrose 5 % (Test B)	segmentation	35	55	50
	traditional	83	100	68

Table 3. Numerical values of the parameters employed

k_s	2.5	W m^{-1} K^{-1}
h	5	W m^{-2} K^{-1}
ρ_{ice}	918	kg m^{-3}
ΔH_f	333500	J kg^{-1}
γb (mannitol)	$7 \cdot 10^4$	J K$^{2/3}$ m$^{-8/3}$
γb (sucrose)	$23 \cdot 10^4$	J K$^{2/3}$ m$^{-8/3}$

Table 4. Mean crystal size for tests A, C, D and E, as evaluated experimentally (traditional technique) and by the simplified model

	Mean crystal size, µm	
	Exp.	Simpl. model
A	24	23
C	29	27
D	35	36
E	22	24

Caption of Figures

Fig. 1. The white pixels have a label k=0. Each black pixel has a label different from zero, with a value which is increasing as we move from left to right on the rows. However, the final value is fixed according to the labels of the black pixels above and on the left of the considered pixel**.**

Fig. 2. A SEM image (left), corresponding to a 5% w/w sucrose solution, is pre-processed to have the binary image (middle) used for segmentation. The segmented image (right) shows super-pixels (here rendered by different colour tones) and their area (in pixels). The image is 300 x 315 pixels (540 x 568 μm).

Fig. 3. Scheme of the domain under investigation.

Fig. 4. (a) SEM and (b) binary images (images are 1024x870 pixels) corresponding to mannitol 5% w/w, test A in Table 2, and (c) the corresponding segmentations where the domains are represented by different colours. The white bar in (a) represents a width of 400 μm. (d) Distribution of the super-pixels (in logarithmic scales), by counting them according to their area (in pixels) within intervals spaced of 100 pixels. Specific data indicated by the arrows in this figure are listed in Table 2. SEM images (Fig. 4a) are adapted with permission from [46]. Copyright 2017 American Chemical Society.

Fig. 5. (a) SEM and (b) binary images corresponding to sucrose 5% w/w, test B in Table 2. The white bar in (a) represents a width of 500 μm. (c) Distribution of the super-pixels (in logarithmic scales), by counting them according to their area (in pixels) within intervals spaced of 100 pixels. Specific data indicated by the arrows in this figure are listed in Table 2.

Fig. 6. Comparison between simplified model predictions (-Δ-) and traditional SEM analysis results (■) for the average crystal size in the case of tests A and B (5% w/w mannitol or sucrose respectively). The histograms refer to the pore size radial distribution observed with SEM analysis. Insets show the temperature profiles at the product bottom as predicted by the model (solid black line) and as measured experimentally (black triangles).

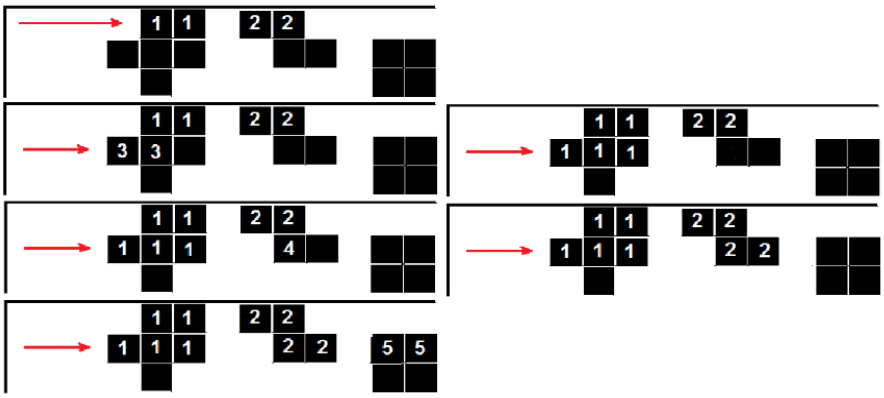

Fig.1

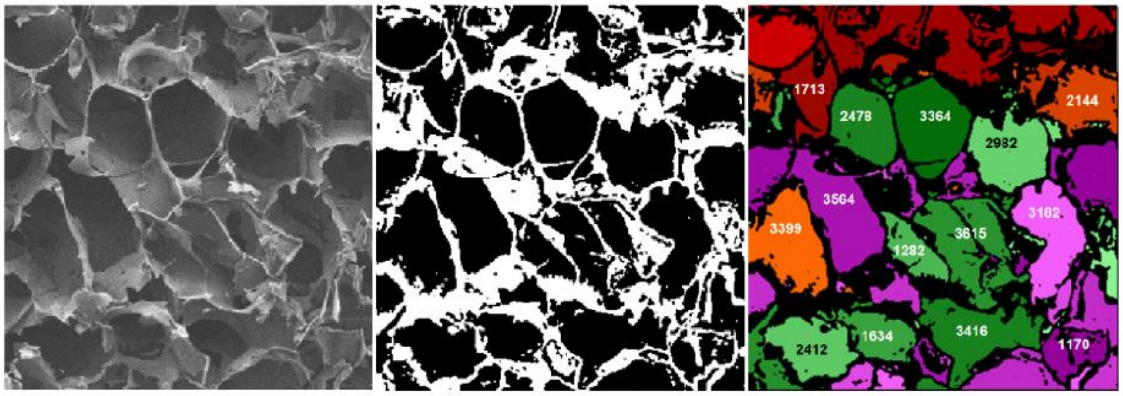

Fig.2

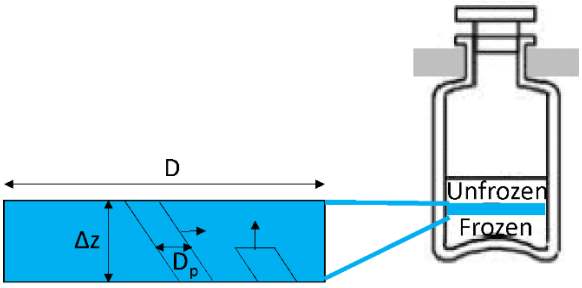

Fig.3

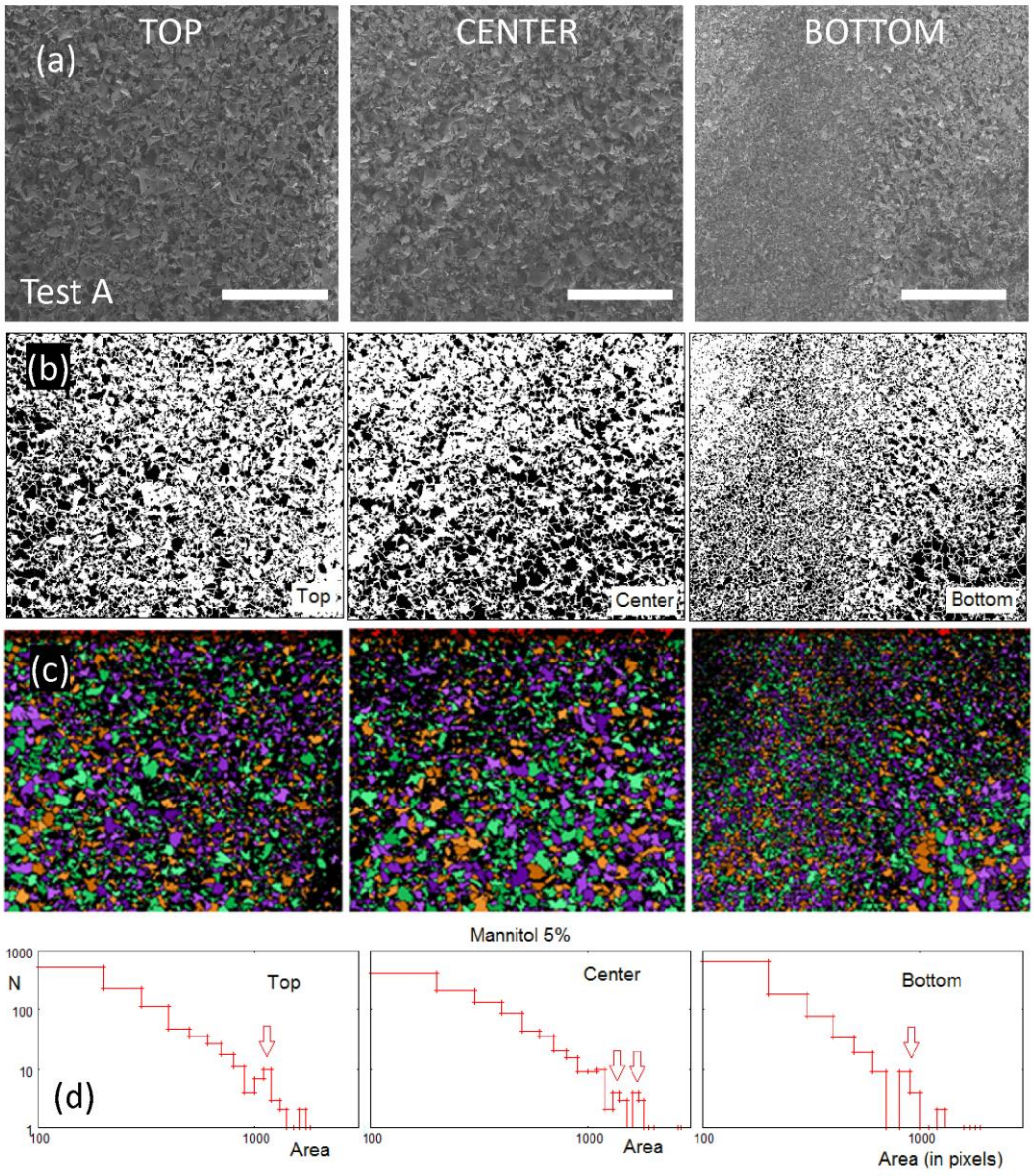
TOP
CENTER
BOTTOM
(a)
Test A
(b)
Top
Center
Bottom
(c)
Mannitol 5%
N
Top
Center
Bottom
(d)
Area
Area
Area (in pixels)

Fig.4

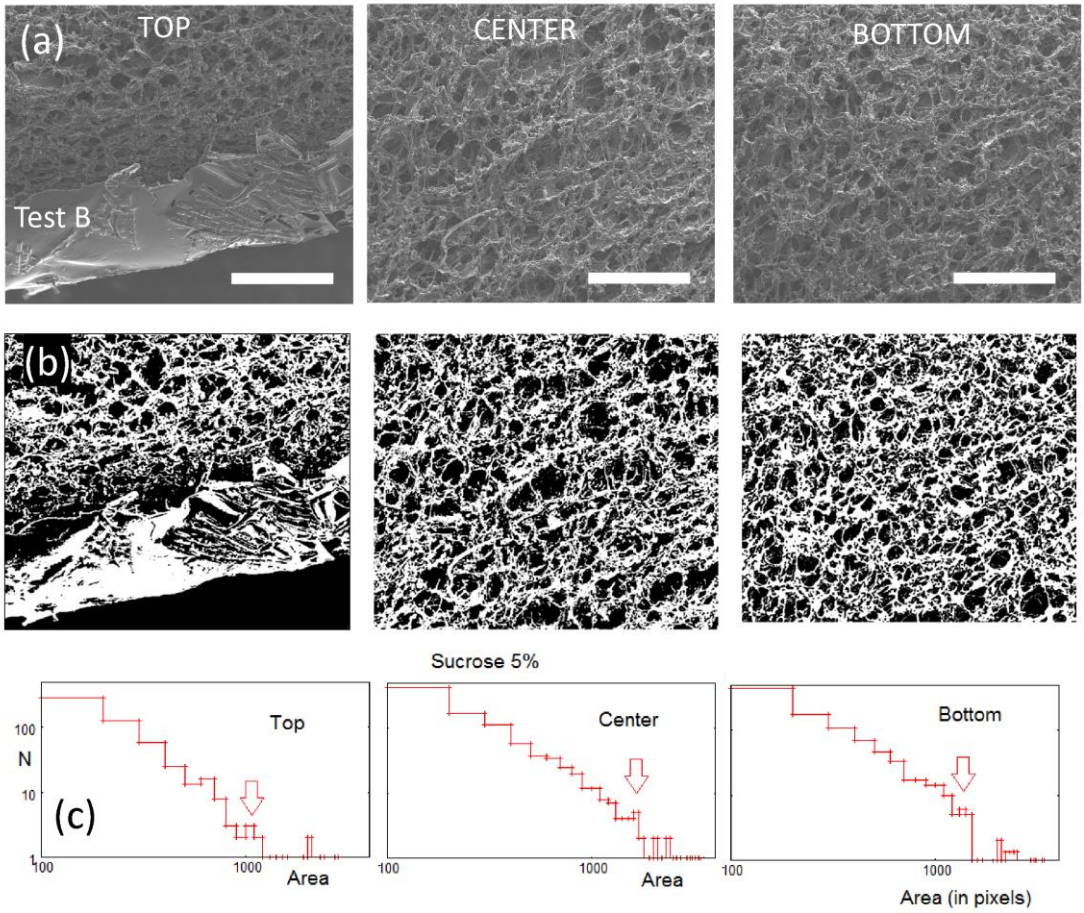
(a)
TOP
CENTER
BOTTOM
Test B
(b)
Sucrose 5%
Top
Center
Bottom
100
N
10
1
(c)
100
1000
Area
Area (in pixels)

Fig.5

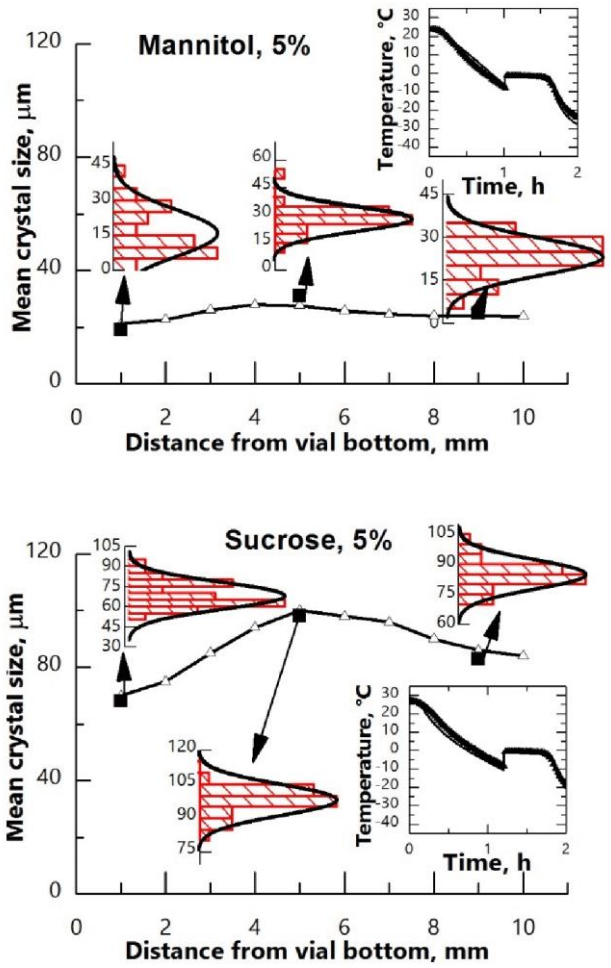
Mannitol, 5%
Mean crystal size, μm
Distance from vial bottom, mm
Temperature, °C
Time, h
Sucrose, 5%
Mean crystal size, μm
Distance from vial bottom, mm
Temperature, °C
Time, h

Fig.6